RSC Advances

PAPER

View Article Online
View Journal | View Issue

Cite this: *RSC Adv.*, 2025, **15**, 31965

Bioassay-guided isolation of terpenoids from the soft coral *Sclerophytum humesi* and assessment of their antidiabetic and cytotoxic activities

Phuong Vu Luu, [a] Quoc-Dung Tran Huynh, [bc] Ngoc-Thac Pham,[d] Huong-Giang Le,[d] Lo-Yun Chen,[d] Cuong-Quoc Nguyen, [e] Huong Lien Ton-Nu, [f] Mei-Hsien Lee, [adg] Yu-Chia Chang, [hi] Jui-Hsin Su, [jk] Bo-Rong Peng*[adi] and Kuei-Hung Lai *[adl]

This study represents the first report on the secondary metabolites from the soft coral *Sclerophytum humesi*. Nine terpenoids (**1–9**) were isolated by antidiabetic-guided isolation, including a new xeniaphyllane-type diterpenoid (Sclerohumin O, **1**) and a new norcaryophyllene-type sesquiterpenoid (Norsclerohumin P, **6**). These compounds feature a distinctive 4/9-fused ring system, which was the first isolated in the *Sclerophytum* genus. All compounds were subjected to evaluation for their antidiabetic and cytotoxic activities. Notably, compound **1** demonstrated substantial inhibitory activity against key metabolic enzymes implicated in diabetes, namely α-amylase, α-glucosidase, and lipase, with IC_{50} values of 100.3 ± 1.02, 170.0 ± 0.92, and 16.1 ± 2.15 μM, respectively. Moreover, compound **1** demonstrated potent cytotoxicity against pancreatic cancer cell lines, with IC_{50} values of 11.01 ± 1.43 μM (MIA PaCa-2), 19.06 ± 0.28 μM (Panc-1), and 17.86 ± 0.87 μM (KPC). Additionally, compounds **3** and **4** showed strong inhibitory activity against the MIA PaCa-2 cell line, with IC_{50} values of 2.52 ± 0.27 μM and 2.54 ± 0.38 μM, respectively. Enzyme kinetics, molecular docking, and molecular dynamics simulations were also performed to further elucidate the experimental findings. These results underscore the potential of marine-derived terpenoids as promising multifunctional bioactive agents with therapeutic applications in the management of diabetes, obesity, and pancreatic cancer.

Received 11th July 2025
Accepted 22nd August 2025

DOI: 10.1039/d5ra04971g

rsc.li/rsc-advances

1. Introduction

Type 2 diabetes mellitus (T2DM), obesity, and pancreatic ductal adenocarcinoma (PDAC) are prominent global health issues associated with substantial morbidity and mortality. Accumulating epidemiological evidence indicates a complex, bidirectional interplay among these conditions, largely mediated through common metabolic, inflammatory, and molecular pathways. Numerous studies have consistently demonstrated that individuals with longstanding non-insulin-dependent diabetes mellitus have a 1.5- to 2-fold increased risk of developing PDAC.[1–4] In the setting of obesity, adipose tissue releases free fatty acids (FFAs), which circulate and accumulate in non-adipose tissues such as liver, muscle, and pancreas, leading to insulin resistance and diabetes. Moreover, adipokines, alterations in gut microbiota, and inflammatory markers may play roles in the development of pancreatic cancer through mechanisms that remain to be fully elucidated. Conversely, new-onset diabetes can serve as an early indicator of subclinical PDAC, illustrating a bidirectional relationship between these conditions (Fig. 1).[5–8] The underlying mechanisms include chronic hyperglycaemia and insulin resistance, which create a pro-inflammatory and oxidative environment that supports

[a]*Graduate Institute of Pharmacognosy, College of Pharmacy, Taipei Medical University, Taipei 110301, Taiwan. E-mail: kueihunglai@tmu.edu.tw; pengpojung@gmail.com*

[b]*Institute of Biological Chemistry, Academia Sinica, Taipei 115, Taiwan, ROC*

[c]*Institute of Pharmaceutical Education and Research, Binh Duong University, Thu Dau Mot, Binh Duong, 820000, Vietnam*

[d]*PhD Program in Clinical Drug Development of Herbal Medicine, College of Pharmacy, Taipei Medical University, Taipei 110301, Taiwan*

[e]*Department of Health Sciences, College of Natural Sciences, Can Tho University, Can Tho, Vietnam*

[f]*Department of Chemistry, College of Natural Sciences, Can Tho University, Can Tho, Vietnam*

[g]*Center for Reproductive Medicine and Sciences, Taipei Medical University Hospital, Taipei 110301, Taiwan*

[h]*Graduate Institute of Healthy Industry Technology, Center for Drug Research and Development, College of Human Ecology, Chang Gung University of Science and Technology, Taoyuan 333324, Taiwan*

[i]*Department of Cosmetic Science, Chang Gung University of Science and Technology, Taoyuan City 33303, Taiwan*

[j]*National Museum of Marine Biology and Aquarium, Pingtung 944401, Taiwan*

[k]*Department of Marine Biotechnology and Resources, National Sun Yat-sen University, Kaohsiung 804201, Taiwan*

[l]*Traditional Herbal Medicine Research Center, Taipei Medical University Hospital, Taipei 110301, Taiwan*

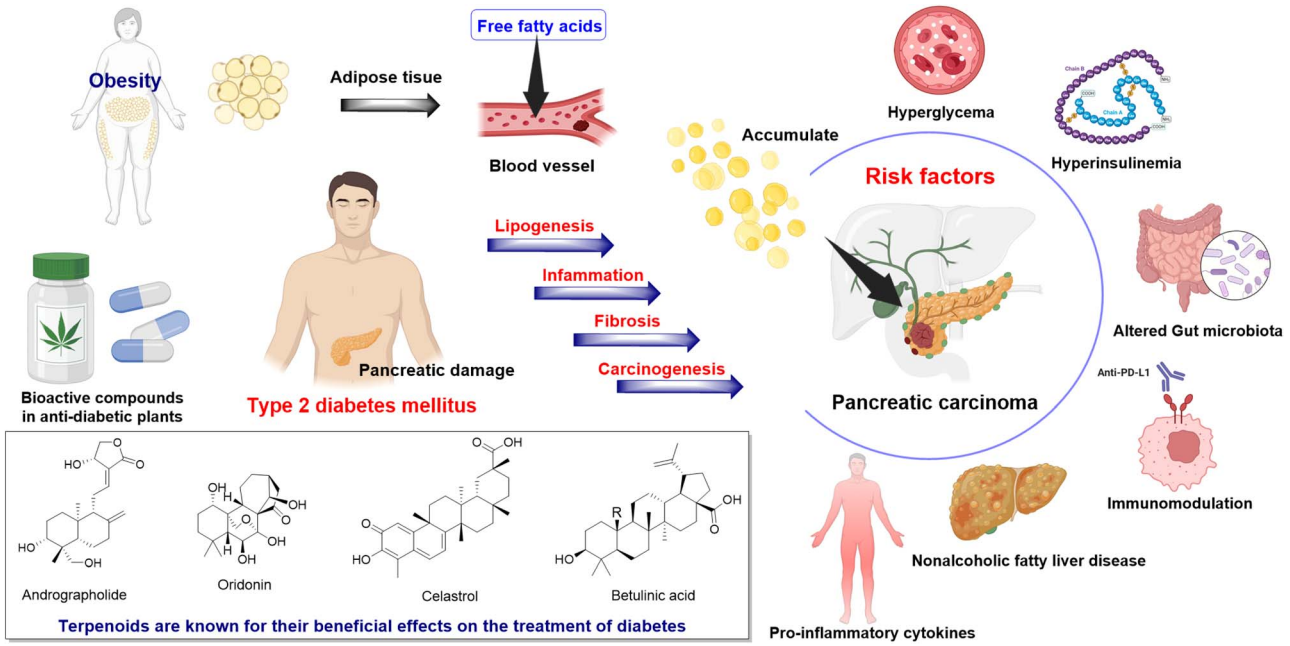

Fig. 1 The relationship between diabetes, obesity, and pancreatic cancer.

carcinogenesis.[9–12] Furthermore, PDAC, along with its precursor lesions like pancreatic intraepithelial neoplasia (PanIN), can cause β-cell dysfunction and apoptosis, leading to impaired insulin secretion and the onset of diabetes.[2,13–16]

An effective therapeutic approach to simultaneously target T2DM and PDAC involves the inhibition of critical digestive enzymes, namely α-amylase, α-glucosidase, and pancreatic lipase. These enzymes play crucial roles in carbohydrate and lipid metabolism, and their inhibition can mitigate postprandial hyperglycemia and dyslipidemia, thereby reducing metabolic stress on pancreatic tissues.[17,18] Terpenoids, a class of natural compounds, have been found to inhibit α-amylase, α-glucosidase, and lipase, while also showing anti-cancer effects on PDAC cells. For instance, andrographolide inhibits α-amylase and α-glucosidase activities and suppresses PDAC cell proliferation by modulating signaling pathways such as NF-κB and β-catenin.[19,20] Similarly, oridonin has been shown to inhibit these enzymes and induce autophagy-mediated cell death in pancreatic cancer models.[21] Betulinic acid exhibits inhibitory effects on α-amylase, α-glucosidase, and lipase, and has been reported to affect energy-related proteomic profiling in PDAC cells, leading to reduced viability and migratory ability.[22,23] Glycyrrhetinic acid also inhibits α-glucosidase and lipase activities and has shown potential anticancer effects.[24] These findings suggest that terpenoids could serve as multi-target agents in the integrated management of T2DT, obesity, and PDAC.

In this investigation, xeniaphyllane-type diterpenoids and norcaryophyllene-type sesquiterpenoids were effectively isolated from the soft coral *Sclerophytum humesi* through a bioassay-guided methodology. These compounds feature a distinctive 4/9-fused ring system, which was the first isolated in the *Sclerophytum* genus. Their inhibitory activities against specific enzymatic targets and cell lines were subsequently evaluated through *in vitro* assays. Moreover, by integrating experimental data with machine learning algorithms, a pharmacological prediction model was developed to facilitate the identification of multi-target inhibitors. These compounds are anticipated to not only modulate postprandial metabolic processes but also exhibit potential anticancer activity against pancreatic ductal adenocarcinoma cells, thereby offering a promising dual-action therapeutic strategy.

2. Materials and methods

2.1. General experimental procedures

The purification and isolation of compounds from the extracts were performed using a series of chromatographic techniques. Fast column chromatography (FCC) was initially conducted using a SepaBean™ machine 2 (China), equipped with either silica gel, to facilitate preliminary fractionation. Subsequently, HPLC was employed to purify the target constituents. Semi-preparative HPLC was carried out on a Shimadzu LC-2050 system (Shimadzu, Kyoto, Japan), utilizing a Galaksil EF-C18-H reverse-phase column (120 Å, 5 μm, 10 × 250 mm; Shimpack GIST PFPP chromatography, China) to achieve high-resolution separation and isolation of the bioactive compounds. Structural elucidation and characterization of the isolated compounds were conducted using a comprehensive suite of spectroscopic techniques. NMR spectroscopy was performed on an Agilent 600 MHz DD2 NMR spectrometer (USA), incorporating both one-dimensional (1D) and two-dimensional (2D) experiments, with methanol-d used as the internal lock solvent to ensure spectral reliability. HR-ESI-MS data were obtained utilizing a SHIMADZU LCMS-9030 system (Japan). IR spectra were recorded employing an IRAffinity-1S FTIR

Spectrometer (Japan). UV spectra were measured using a U-3310 UV-Vis spectrophotometer (Japan). ECD spectra were obtained with a JASCO J-715 spectropolarimeter, and optical rotation values were determined in methanol using a JASCO P-2000 polarimeter (Japan). PDAC cell lines, namely MIA PaCa-2 (CRL-1420) and Panc-1 (CRL-1469), were procured from the American Type Culture Collection (ATCC). The KPC cell line was obtained from the Bioresource Collection and Research Center (Taiwan).

2.2. Animal material

Specimens of the soft coral *Sclerophytum humesi* (voucher specimen no. SH-2023) were collected by scuba diving at a depth of approximately 10–15 meters off the coast of Pingtung County, Taiwan, in November 2023. To preserve the chemical constituents and structural integrity, the samples were immediately frozen upon collection. A voucher specimen has been deposited and archived in the herbarium of the College of Pharmacy, Taipei Medical University (Taipei, Taiwan).

2.3. Extraction and bioassay-guided isolation

The frozen dry specimen of *Sclerophytum humesi* (300 g) underwent thorough extraction using ethyl acetate (EtOAc) at room temperature. The resulting extracts were evaporated under reduced pressure to obtain a brown residue (SH-EA), which weighed 18.1 g.

The SH-EA (18.1 g) was subjected to fractionation using silica gel-FCC with a stepwise gradient elution. The separation was performed at a flow rate of 20 mL min^{-1} over a period of 180 minutes, utilizing a solvent system composed of *n*-hexane (Hex) and EtOAc. The elution gradient gradually transitioned from Hex : EtOAc (100 : 0) to (0 : 100) to obtain eleven fractions (fraction 1–11). All fractions were screened for their antidiabetic activity *via* enzyme inhibition assays targeting α-amylase and α-glucosidase. The results indicated that fraction 5 demonstrated the most potent inhibitory activity. Consequently, fraction 5 (453.2 mg) was selected for further purification, which was carried out using RP-HPLC with an isocratic elution system. The mobile phase consisted of a mixture of acidic water (0.1% formic acid) and acetonitrile in a 40 : 60 ratio. Photodiode array (PDA) detection was carried out at wavelengths of 210 nm and 254 nm, resulting in the collection of seven subfractions (5A–5G). Subfraction 5B (40.5 mg) was purified by reversed-phase chromatography on an EF-C18-H column under isocratic conditions, employing a mobile phase composed of 35% methanol (MeOH) in acidified water at a flow rate of 2 mL min^{-1}. This procedure afforded compound **7** (3.15 mg, t_R = 24.3 min), compound **8** (3.82 mg, t_R = 25.6 min), and compound **9** (4.25 mg, t_R = 26.2 min). Further purification of subfraction 5D (50.6 mg) was performed using a PFPP reversed-phase column under isocratic conditions (45% MeOH) at a flow rate of 2 mL min^{-1}, resulting in the isolation of compound **1** (1.37 mg, t_R = 20.2 min), compound **2** (2.55 mg, t_R = 20.9 min), and compound **3** (2.23 mg, t_R = 23.6 min). Subfraction 5F (20.38

Table 1 ^{1}H and ^{13}C NMR of compounds **1** and **6**

	1[a]		**6**[a]	
No.	δ_H mult. (*J* Hz)	δ_C mult.	δ_H mult. (*J* Hz)	δ_C mult.
1	2.07 m	46.4 CH	2.36 m	57.7 CH
2α	2.14 m	30.2 CH_2	2.48 m	26.4 CH_2
2β	2.31 td (12.5, 7.7)		2.07 m	
3	5.59 m	125.5 CH	5.43 ddd (7.6, 5.7, 1.5)	125.7 CH
4		140.3 qC		139.5 qC
5	4.75 dd (11.6, 5.6)	70.1 CH	1.78 m	37.4 CH_2
6	1.57 tdd (13.0, 5.6, 1.7)	34.9 CH_2	4.51 m	69.9 CH
	1.73 dddd (13.4, 11.6, 6.8, 1.8)			
7α	1.87 dd (14.4, 12.4)	33.2 CH_2	1.79 m	33.4 CH_2
7β	2.19 m		2.37 m	
8		155.0 qC		153.9 qC
9	2.87 m	42.7 CH	1.91 m	40.1 CH
10	2.11 m	35.7 CH_2	1.88 m	40.7 CH_2
11		48.0 qC		71.4 qC
12		206.0 qC	1.19 s	21.8 CH_3
13	6.48 d (15.5)	121.5 CH		
14	6.94 d (15.5)	155.6 CH	4.90 m	110.9 CH_2
15		71.5 qC	1.66 t (1.6)	17.1, CH_3
16	1.32 s	29.3 CH_3		
17	1.32 s	29.3 CH_3		
18	1.33 s	18.2 CH_3		
19	4.54 t (2.2)	110.6 CH_2		
	4.78 q (2.0)			
20	1.64 t (1.1)	16.1 CH_3		

[a] Spectra were acquired at 600 MHz (^{1}H NMR) and 150 MHz (^{13}C NMR) in CD_3OD.

mg) was performed using a reversed-phase chromatography method with a MeOH–water (45 : 55, v/v) mobile phase, resulting in the isolation of compound **4** (5.84 mg, t_R = 25.9 min), compound **5** (2.54 mg, t_R = 26.2 min), and compound **6** (1.23 mg, t_R = 26.8 min).

Sclerohumin O (**1**): colerless oil; $[\alpha]_D^{25}$ −6.8 (*c* 0.1, MeOH); UV (MeOH) λ_{max} (log ε) 246 (0.71), 322 (0.22) nm; IR ν_{max} (MeOH) 3441, 2970, 2931, 2870, 1681, 1627, 1442, 1373, 1311, 1265, 1056 cm^{-1}; HR-ESI-MS *m*/*z* 319.2265 (calculated for $C_{20}H_{31}O_3$, 319.2268, $[M + H]^+$); ^1H (600 MHz, CD_3OD) and ^{13}C (150 MHz, CD_3OD) NMR data are presented in Table 1.

Norsclerohumin P (**6**): colerless oil; $[\alpha]_D^{25}$ +13.3 (*c* 0.1, MeOH); UV (MeOH) λ_{max} (log ε) 228 (0.79) nm; IR ν_{max} (MeOH) 3340, 2962, 2931, 1635, 1450, 1373, 1242, 1211 cm^{-1}; HR-ESI-MS *m*/*z* 223.1692 (calculated for $C_{14}H_{23}O_2$, 223.1693, $[M + H]^+$); ^1H (600 MHz, CD_3OD) and ^{13}C (150 MHz, CD_3OD) NMR data are presented in Table 1.

2.4. NMR and ECD calculations

Compounds **1** and **6** underwent comprehensive conformational analysis to elucidate their stereochemical configurations and predict spectroscopic properties. Initially, conformers for each stereochemical configuration were generated within an energy range of 3.5 kcal mol^{-1} using the GMMX method implemented in GaussView 6.1 (USA). These conformers underwent geometry optimization and vibrational frequency analysis at the B3LYP/6-31G(d,p) level of theory, incorporating MeOH as the solvent, using Gaussian 16 software. All conformers, confirmed as true minima, showed no imaginary frequencies. The Gibbs free energy for each conformer was computed to assess their Boltzmann populations, and those with populations below 2% were omitted from further analysis. Remaining conformers were used for NMR chemical shift calculations *via* Gauge-Including Atomic Orbital (GIAO) DFT at the MPW1PW91/6-311+G(d,p) level with the IEFPCM model for MeOH, applying the DP4+ prediction method. Unscaled chemical shifts (δ_u) were obtained relative to tetramethylsilane (TMS), using the equation $\delta_u = \sigma_0 - \sigma_x$, where σ_x is the Boltzmann-averaged shielding tensor of all significant conformers, and σ_0 is the TMS shielding tensor computed at the same level. The averaged chemical shifts, weighted by conformer populations, were analyzed with Excel and the DP4+ approach. For ECD calculations, the excitation energies of the lowest 30 electronic states were obtained using DFT/B3LYP/6-311++G(d,p) with a solvent model in Gaussian 16. The overall ECD spectra for all conformers were then generated by weighting according to their Boltzmann distributions, employing SpecDis 1.71 with a broadening parameter (σ) of 0.30 eV. The computed spectra were subsequently analyzed alongside the experimental CD measurements, which were recorded over a wavelength range of 200–400 nm, consisting of 301 data points, with CD values expressed in millidegrees (mdeg).

2.5. Antidiabetic activity

2.5.1. Anti-α-amylase assay. The α-amylase inhibitory activity was evaluated using a standard method with slight modifications.[25] The 50 μL of phosphate buffer (pH 6.8), 50 μL of α-amylase enzyme solution (3 U mL^{-1}), and 50 μL of the test compound were mixed and incubated at 37 °C for 15 minutes. After incubation, 100 μL of a starch solution (2 mg mL^{-1}) was added to the reaction mixture, followed by further incubation at 37 °C for 15 minutes. The reaction was subsequently terminated by the addition of 50 μL of dinitro salicylic acid (DNS) reagent to quantify reducing sugars. Absorbance readings were taken at 540 nm using a UV-Vis spectrophotometer. A control sample lacking any test compound served as the reference. The half-maximal inhibitory concentration (IC_{50}) values were determined from dose–response curves *via* non-linear regression analysis.

2.5.2. Anti-α-glucosidase assay. The α-glucosidase inhibitory assay was conducted following a previously described protocol with minor modifications.[26] The reaction was carried out in 50 mM NaH_2PO_4 (pH 6.8). In a 96-well microplate, 30 μL of the test sample and 25 μL of enzyme (0.2 U mL^{-1}) prepared in buffer, combined and incubated at room temperature for 20 minutes. Finally, 25 μL of *p*-nitrophenyl-α-D-glucopyranoside substrate solution, also prepared in buffer, was added to initiate the enzymatic reaction. The plate was further incubated for an additional 10 minutes. The reaction was stopped by adding 50 μL of 0.2 M sodium carbonate (Na_2CO_3) to each well. The absorbance of the released *p*-nitrophenol was measured at 405 nm.

2.5.3. Anti-lypase assay. The inhibitory activity against pancreatic lipase was evaluated based on a modified version of previously reported protocols.[25] In each assay, 5 μL of the test sample was added to a mixture containing 250 μL of *p*-nitrophenyl palmitate (*p*NPP, 20 mM dissolved in acetonitrile). The mixture was preincubated at 37 °C for 5 minutes. Subsequently, the reaction was initiated by adding 250 μL of porcine pancreatic lipase solution, prepared in Tris–HCl buffer. The final reaction mixture was incubated at 37 °C for 15 minutes. The enzymatic reaction was terminated by adding 1000 μL of 200 mM sodium carbonate (Na_2CO_3). The release of *p*-nitrophenol, which indicates lipase activity, was quantified by measuring the absorbance at 405 nm using a UV-Vis spectrophotometer.

2.5.4. Enzyme kinetic assay. Kinetic studies were conducted by varying the substrate concentrations, soluble starch for α-amylase and *p*NPP for pancreatic lipase, in the absence and presence of the test compound at different concentrations. Lineweaver–Burk plots (1/*V* *versus* 1/[S]) were constructed to determine the mode of enzyme inhibition exerted by the compounds.

$$\frac{1}{V_0} = \frac{K_m}{V_{max}} \times \frac{1}{[S]} + \frac{1}{V_{max}}$$

Furthermore, the inhibition constant (K_i), which reflects the binding affinity and potency of the inhibitor, was calculated from secondary plots of the slope values against the inhibitor concentrations [I]. The experimental protocols and analytical methods were adapted from previously published studies, with slight modifications to the concentration ranges tested.[27,28]

2.6. Theoretical studies

All theoretical computational protocols were performed and analyzed following recently published studies.[29–34] Specifically, the stable conformations of the ligands were optimized using Gaussian 09 software. Full geometry optimizations were carried out employing the B3LYP functional combined with the 6-31G(d,p). The crystal structures of α-amylase (PDB ID: 1B2Y)[35] and lipase (PDB ID: 1EX9)[36] were retrieved from the RCSB Protein Data Bank (https://www.rcsb.org/). All water molecules and small co-crystallized ligands were removed using Discovery Studio Visualizer. Molecular docking studies were conducted using LeadIT software. Grid box parameters were defined to cover all residues surrounding the enzyme active site. Following docking, fifty ligand poses complexed with the receptor were generated and ranked according to their docking scores and binding energies, expressed in kJ mol^{-1}. Molecular dynamics simulations were conducted using the Desmond package. The protein–ligand complexes were solvated employing the single point charge (SPC) water model, and system neutrality was ensured by neutralizing the total charge. Simulations were carried out using default parameters. Equilibration of the system was performed under isothermal–isobaric (NPT) ensemble conditions, yielding simulation trajectories for subsequent analyses.

2.7. Cell viability assay

The experimental protocols and analytical methodologies were adapted from previously published studies, incorporating minor modifications to the tested concentration ranges.[37–39] The cells were cultured in Dulbecco's Modified Eagle Medium (DMEM, Gibco) supplemented with 10% Fetal Bovine Serum (FBS, Gibco) and 1% antibiotic–antimycotic solution (Gibco). Upon reaching approximately 80% confluence, the cells were washed with phosphate-buffered saline (PBS) and detached using 0.25% trypsin-0.02% EDTA (Gibco) at 37 °C for 5 minutes. The detached cells were then seeded into 96-well plates at a density of 3×10^4 cells per well in 100 μL of fresh medium and incubated at 37 °C with 5% CO_2 for 24 hours. Subsequently, 100 μL of fresh medium containing the test compounds was added to each well, and the cells were incubated for an additional 72 hours. Cell viability was assessed using the Cell Counting Kit-8 (CCK-8) assay according to the manufacturer's instructions. Absorbance was measured at 450 nm using a microplate reader. Cell viability was determined using the following formula:

$$(\%)\ \text{Cell viability} = [(\text{Abs}_{\text{sample}} - \text{Abs}_{\text{blank}})/(\text{Abs}_{\text{control}} - \text{Abs}_{\text{blank}})] \times 100\%$$

Compounds demonstrating greater than 50% cytotoxicity were subjected to further analysis to determine their IC_{50} values. Gemcitabine was employed as a positive control in these assays.

2.8. Statistical analysis

Statistical evaluations for the *in vitro* studies were performed using GraphPad Prism version 8.0.2. Results are presented as the mean ± standard deviation (SD). The data were analyzed through a one-way analysis of variance (ANOVA), with subsequent Tukey's post hoc test for multiple comparisons. A *P*-value below 0.05 was regarded as statistically significant.

3. Result and discussion

3.1. Bioassay-guided isolation and structure elucidation

The ethyl acetate-soluble fraction of the crude extract obtained from the soft coral was subjected to successive flash chromatography on silica gel, yielding eleven fractions. Fractions 1–11 were screened for their antidiabetic activity *via* inhibition assays against the enzymes α-amylase and α-glucosidase. The results demonstrated that fraction 5 exhibited the most potent inhibitory activity (Fig. 2). Consequently, fraction 5 was further purified, resulting in the isolation of two new compounds (**1** and **6**) and seven known compounds (**2–5**, **7–9**) (Fig. 3).

Sclerohumin O (**1**) was isolated as an optical, colorless oil. HR-ESI-MS analysis revealed a protonated molecular ion $[M + H]^+$ at *m*/*z* 319.2265, consistent with the molecular formula $C_{20}H_{30}O_3$ (calculated *m*/*z* 319.2268, $C_{20}H_{31}O_3$). This molecular composition indicates six degrees of unsaturation. The IR spectrum of compound **1** showed typical absorption indicative of a hydroxy group (ν_{max} 3441 cm^{-1}) and a conjugated carbonyl

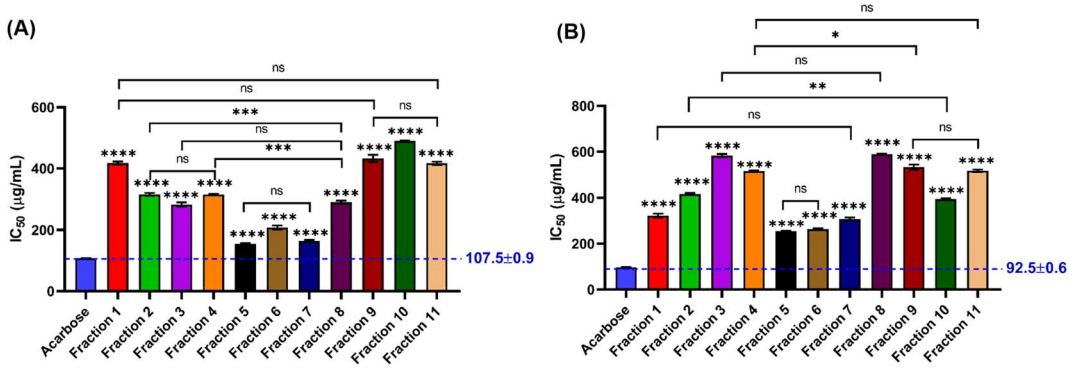

Fig. 2 *In vitro* inhibitory activities of *Sclerophytum humesi* fractions against α-amylase (A) and α-glucosidase enzymes (B). The data are presented as the mean ± SD with $n = 3$. *$p < 0.05$, **$p < 0.01$, ***$p < 0.001$ and ****$p < 0.0001$ compared to positive control.

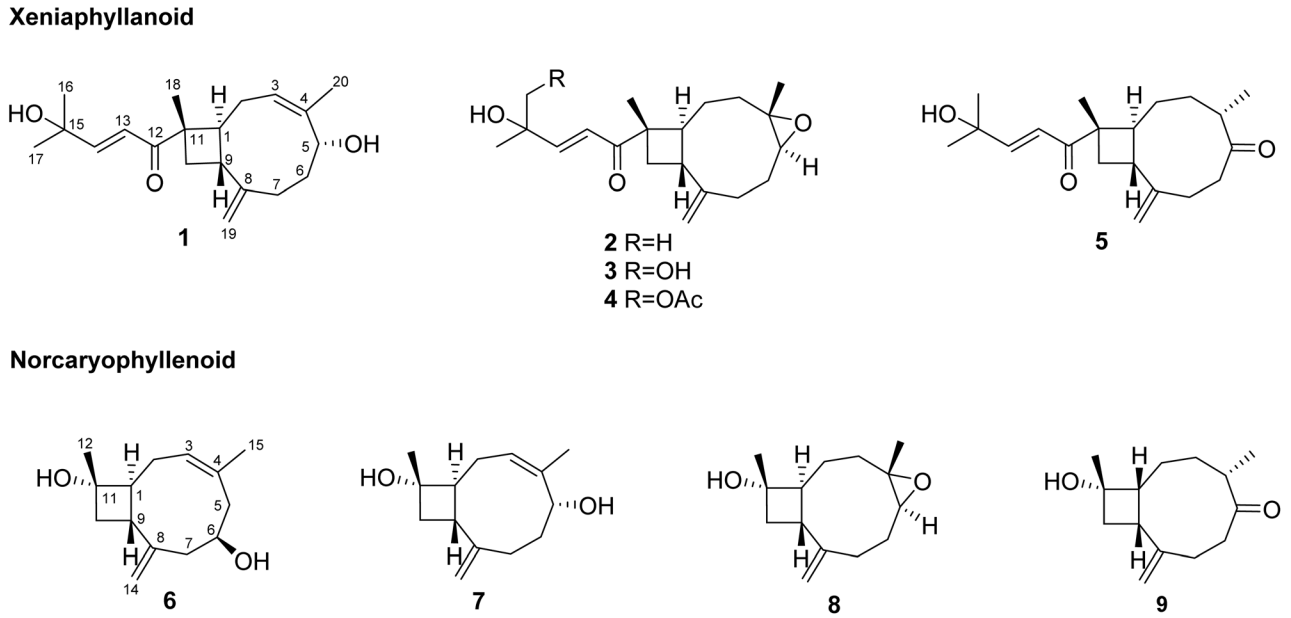

Fig. 3 Chemical structure of compounds **1**–**9**.

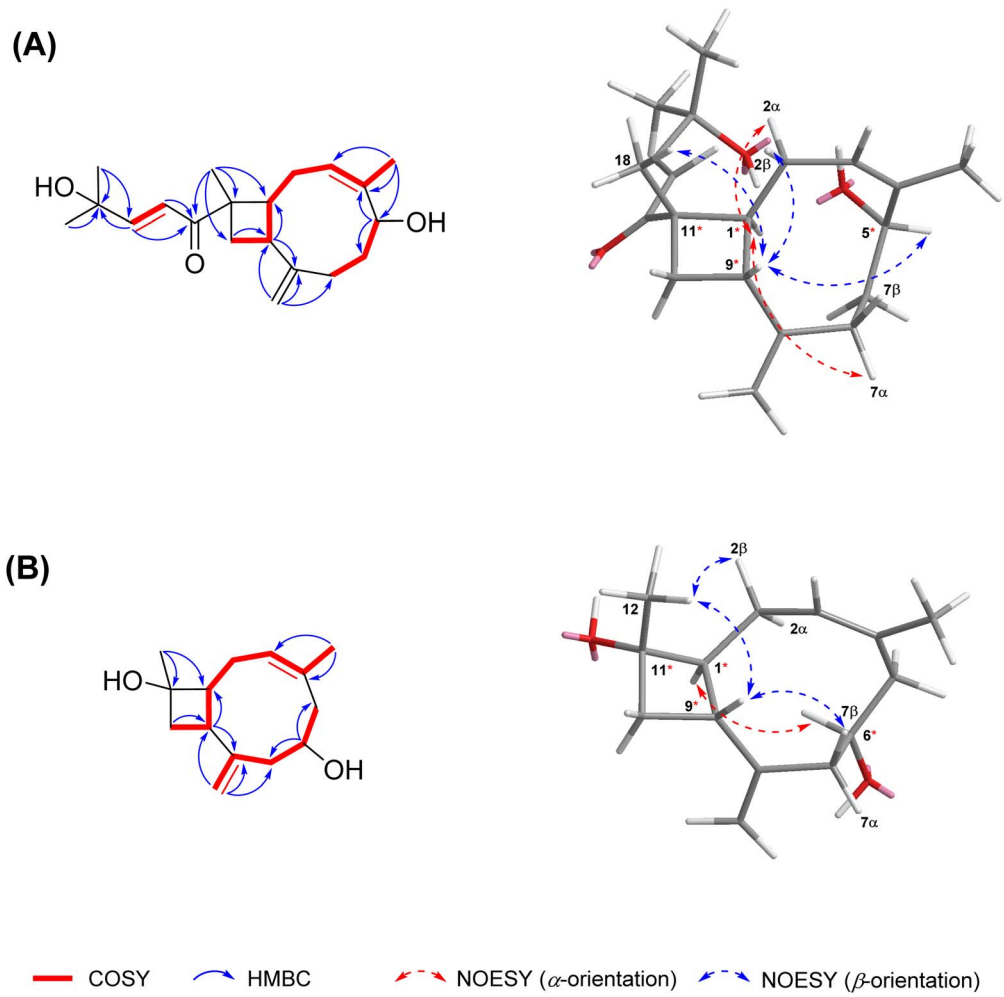

Fig. 4 Significant COSY, HMBC, and NOESY correlations observed in **1** (A), and **6** (B).

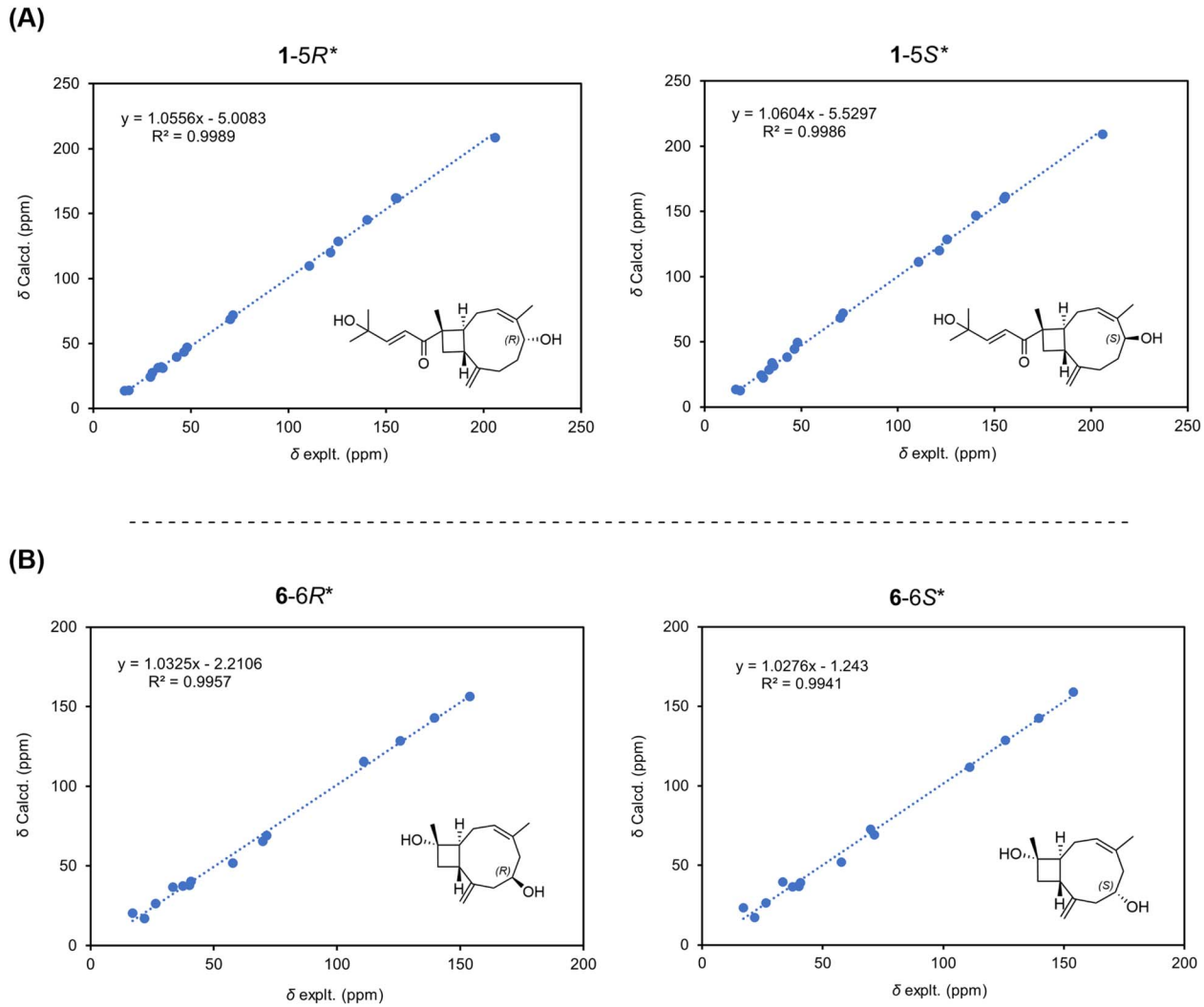

Fig. 5 Linear correlations of the calculated **1**-5*R** and **1**-5*S** (A), **6**-6*R** and **6**-6*S** (B) with the experimentally observed ^{13}C NMR chemical shifts.

group (ν_{max} 1681 cm^{-1}). Analysis of the 1D NMR data (Table 1) of **1** was similar to those of compound **2**, nanolobatin B,[40] except that an olefinic group was present at Δ^3 [δ_H 5.59 (*m*, H-3); δ_C 125.5, C-3; δ_C 140.3, C-4] and the oxygenated methine group at [δ_H 4.75 (dd, J = 11.6, 5.6 Hz, H-5); δ_C 70.1, C-5]. This deduction was supported by COSY cross-peaks between H_2-10/H-9/H-1/H_2-2/H-3/H_3-20 and H-5/H_2-6/H_2-7, together with the key HMBC from H_3-20 to C-3, C-4, and C-5, as well as from H-5 to C-4 and C-6 (Fig. 4A). The relative configuration of **1** was elucidated through key NOESY correlations, notably between H_3-18 (δ_H 1.33)/H-9 (δ_H 2.87), H-9/H-5 (δ_H 4.75), H-9/H_2-2β (δ_H 2.31), H-1 (δ_H 2.07)/H_2-2α (δ_H 2.14), and H-1/H_2-7α (δ_H 1.87), indicating that H_3-18, H-5, and H-9 possessed a β-orientation, while H-1 was α-oriented (Fig. 4A).[40–42] Therefore, the relative configuration of **1** was established as 1*S**, 5*R**, 9*R**, 11*S**. However, due to the conformational flexibility of the cyclononane ring, which may render NOESY interactions between distant protons less reliable, GIAO-NMR calculations were employed for further confirmation. Two possible stereoisomers, **1a**-(1*S**, 5*R**, 9*R**, 11*S**) and **1b**-(1*S**, 5*S**, 9*R**, 11*S**), were evaluated. The correlation coefficient (R^2) obtained from linear regression analysis between the theoretical values for 5*R**-**1a** and the experimental

Table 2 Comparative analysis of the stereochemical assignments for **1**-5*R** and **1**-5*S** utilizing DP4+ (DFT)/MPW1PW91/6-311+G (d,p) level

		sDP4+		uDP4+		DP4+	
Exp. NMR	Nuclei	**1**-5*R**	**1**-5*S**	**1**-5*R**	**1**-5*S**	**1**-5*R**	**1**-5*S**
1	^{1}H	100%	0.00%	100%	0.00%	100%	0.00%
	^{13}C	97.79%	2.21%	29.04%	70.96%	94.76%	5.24%
	All data	100%	0.00%	99.99%	0.01%	100%	0.00%

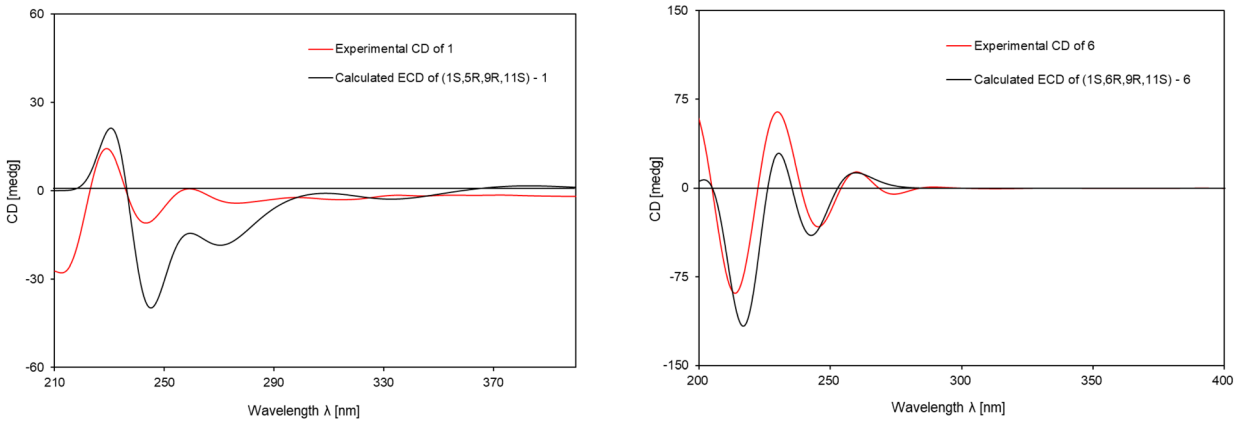

Fig. 6 Comparative analysis of the experimental ECD spectra of compounds **1** and **6** with the corresponding calculated spectra.

Table 3 Comparative analysis of the stereochemical assignments for **6**-6*R** and **6**-6*S** utilizing DP4+ (DFT/MPW1PW91/6-311+G (d,p)) level

		sDP4+		uDP4+		DP4+	
Exp. NMR	Nuclei	**6**-6*R**	**6**-6*S**	**6**-6*R**	**6**-6*S**	**6**-6*R**	**6**-6*S**
6	^{1}H	86.17%	13.83%	49.61%	50.39%	85.99%	14.01%
	^{13}C	94.08%	5.92%	52.20%	47.80%	94.55%	5.45%
	All data	99.00%	1.00%	51.81%	48.19%	99.07%	0.93%

data for **1** was 0.9989. In comparison, the R^2 value for 5*S**-**1b** relative to **1** was determined to be 0.9986 (Fig. 5A). These results were subsequently assessed using DP4+ methods, which yielded a match ratio of 100.00% (all data) for 5*R**-**1a**, respectively (Table 2). The absolute configuration of **1** was conclusively determined as 1*S*, 5*R*, 9*R*, 11*S* through time-dependent density functional theory (TDDFT) calculations of its electronic circular dichroism (ECD) spectrum (Fig. 6). The calculated Boltzmann-averaged ECD spectrum closely matched the experimental data, validating the assigned stereochemistry.

Norslerohumin P (**6**) was obtained as a colorless oil and possessed the molecular formula $C_{14}H_{22}O_2$ as assigned by HR-ESI-MS pseudo-molecular ion peak $[M + H]^+$ at *m*/*z* 223.1692 (calculated *m*/*z* 223.1693, $C_{14}H_{23}O_2$). The NMR data of compound **6** were closely with those of compound **7**, except that the hydroxyl group at C-6 [δ_H 4.51 (*m*, H-6); δ_C 69.9, C-6].[43] This planar structure of **6** was elucidated through comprehensive ^{1}H–^{1}H COSY correlations revealed key interactions between H_2-5/H-6/H_2-7/H_2-14, along with the key HMBC from H-6 to C-5, C-7 (Fig. 4B). The relative configuration of **6** was established by the NOESY experiment. The key NOESY correlations between H_3-12 (δ_H 1.19)/H-9 (δ_H 1.91), H_3-12/H_2-2β (δ_H 2.07), and H-9/H_2-7β (δ_H 2.37), as well as H-1 (δ_H 2.36)/H-6 (δ_H 4.55), support the assignment of the relative β-orientation for H_3-12 and H-9. Conversely, H-1 and H-6 were determined to adopt an α-orientation (Fig. 4B). As a result, the relative configuration of **6** was determined to be 1*S**, 6*R**, 9*R**, 11*S**. Similarly to **1**, GIAO-NMR calculations were employed to achieve more definitive structural confirmation. Two plausible configurations, **6a**-(1*S**, 6*R**, 9*R**, 11*S**) and **6b**-(1*S**, 6*S**, 9*R**, 11*S**), were computationally evaluated, with configuration **6a** demonstrating superior agreement (99.07%) (Table 3). This result supports the assignment of the relative configuration of **6** as 1*S**, 6*R**, 9*R**, 11*S** (Fig. 5B). To further substantiate the absolute configuration of **6**, TDDFT-ECD calculations were conducted. The Boltzmann-averaged ECD spectrum of (1*S*, 6*R*, 9*R*, 11*S*)-**6** shows a strong correlation with the experimental ECD curve of **6** (Fig. 6), thereby confirming the absolute configuration assignment as 1*S*, 6*R*, 9*R*, 11*S*.

The structures of the isolated known compounds, nanolobatin B (**2**),[40] gibberosin G (**3**),[41] gibberosin H (**4**),[41] sinuhirtin E (**5**),[44] sinunorcaryophyllenol (**7**),[43] nanorcaryophyllene A (**8**),[42]

Table 4 *In vitro* antidiabetic activity

	IC_{50} (μM)		
Samples	α-amylase	α-glucosidase	Lypase
1	**100.3 ± 1.02**	**170.0 ± 0.92**	**16.1 ± 2.15**
2	207.2 ± 1.48	241.8 ± 1.11	153.0 ± 3.01
3	210.2 ± 1.30	319.7 ± 1.02	193.0 ± 1.01
4	371.5 ± 1.77	462.7 ± 2.42	425.0 ± 2.91
5	**95.5 ± 0.99**	253.3 ± 0.88	**16.9 ± 1.20**
6	>500	498.2 ± 1.95	>500
7	>500	>500	>500
8	>500	>500	>500
9	>500	>500	>500
Acarbose[a]	165.8 ± 1.03	144.0 ± 1.99	NT
Orlistat[b]	NT	NT	14.2 ± 0.31

[a] Active ingredient acarbose (Domesco, Vietnam). [b] Orlistat in Orlistat STADA (Stella Pharm, Germany) were used for the positive control. NT: not tested.

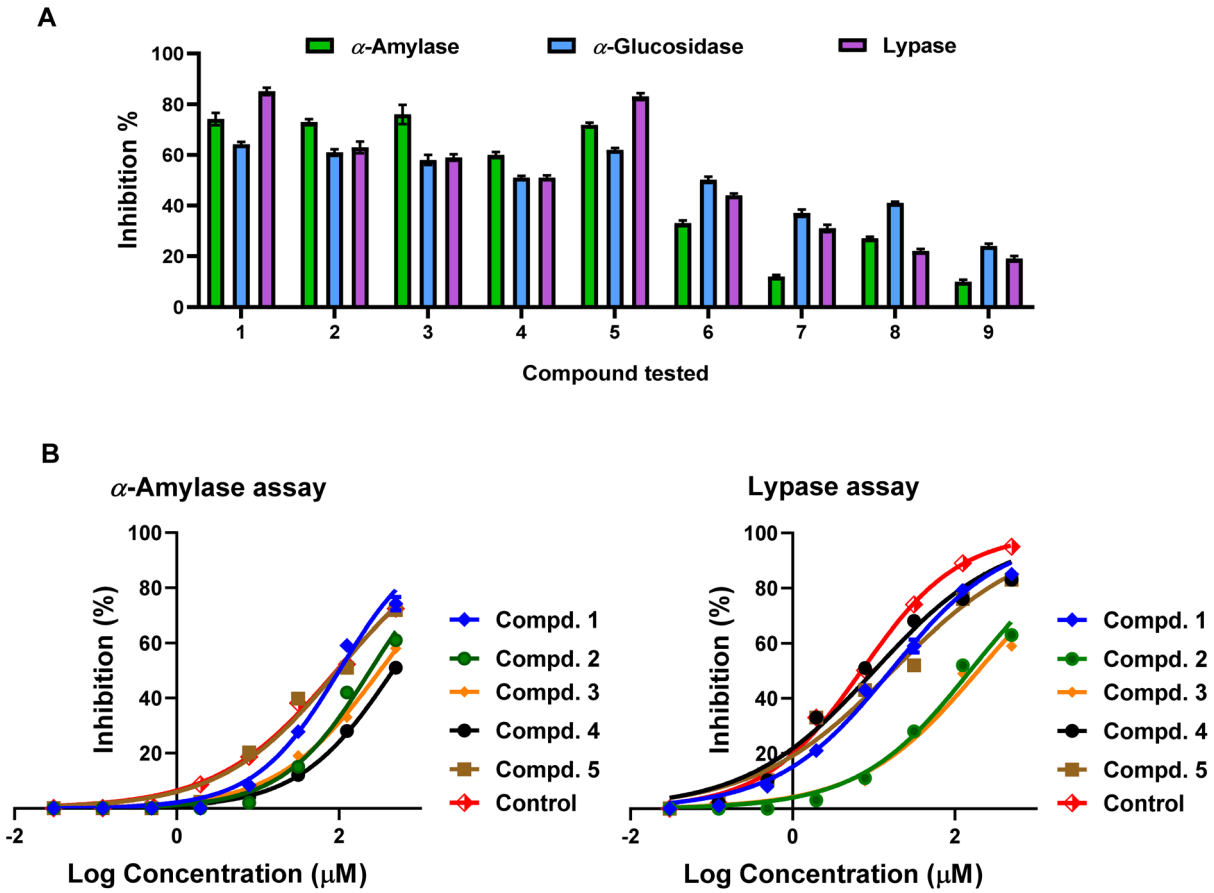

Fig. 7 The percentage inhibition of α-amylase, α-glucosidase, and lipase by compounds **1–9** isolated from *Sclerophytum humesi* at a concentration of 500 μM (A). Dose–response curves of the potent inhibitory compounds **1–5** against α-amylase and lipase (B).

and nanorcaryophyllene B (**9**),[42] were confirmed (Fig. 2) through comparison with existing literature references, including 1D NMR and ESI-MS.

3.2. Antidiabetic activity

In vitro bioassays demonstrated that compounds **1–9** exhibited significant inhibitory activities against α-amylase, α-glucosidase, and pancreatic lipase-key enzymes implicated in the management of type 2 diabetes (Table 4 and Fig. 7). Among these, compounds **1** and **5** emerged as promising dual-target inhibitors, warranting further detailed investigation.

Specifically, in the α-amylase inhibition assay, compound **5** showed the most potent activity with an IC_{50} value of 95.5 ± 0.99 μM, followed closely by compound **1** with an IC_{50} of 100.3 ± 1.02 μM. Both compounds exhibited stronger inhibition than the positive control acarbose (IC_{50} = 165.8 ± 1.03 μM), indicating potential efficacy in modulating postprandial glucose levels. To elucidate the inhibitory mechanism, Lineweaver–Burk plots were generated by graphing the reciprocal of reaction velocity ($1/V$) *versus* the reciprocal of substrate concentration (1/[S]), both in the presence and absence of compounds **1** and **5**. Both compounds acted as non-competitive inhibitors of α-amylase. The inhibition constants (K_i) determined from slope replots were 91.7 μM for compound **1** and 25.6 μM for compound **5**. Molecular docking and dynamics simulations further clarified the binding mechanisms of these compounds to α-amylase. Compound **1** displayed strong binding affinity (−10.16 kJ mol^{-1}) at the enzyme's active site through multiple interactions, including H-bond donor (HBD) between the –OH linked bicyclo[7.2.0]undecane ring system with His305, pi–sigma interaction with Tyr62, and several pi–alkyl contacts with aliphatic residues such as Leu162, Ala198, Ile236, and His201. Compound **5** formed H-bond acceptor (HBA) interactions between its –C=O-linked bicyclo[7.2.0]undecane ring with Gly306, as well as HBD at the C^{15}–OH with Trp59, along with pi–alkyl interactions involving Trp59 and Leu165 (Fig. 8C).

Dynamic simulations revealed stable ligand–enzyme complexes over 100 ns in aqueous solution at pH 7.4. The **1**-amylase complex stabilized after 50 ns, RMSD fluctuating between 0.8 and 1.1 Å. Conversely, the **5**-amylase complex displayed initial instability during the first 40 ns (RMSD ranging from 0.3 to 2.1 Å) but stabilized thereafter, maintaining RMSD between 1.0 and 1.8 Å (Fig. 9C). Notably, molecular dynamics revealed protein–ligand contacts with hydrophobic residues such as C^{12}=O–Arg195 (43%), C^{12}=O–Asp197 (94%), and –C^{15}–OH–HOH–Asp300 (64%), alongside hydrophobic interactions with key amino acids. The **5**-amylase complex similarly formed H-bond with C^{12}=O–HOH–Leu162 (32%), –C^{5}=O–HOH–

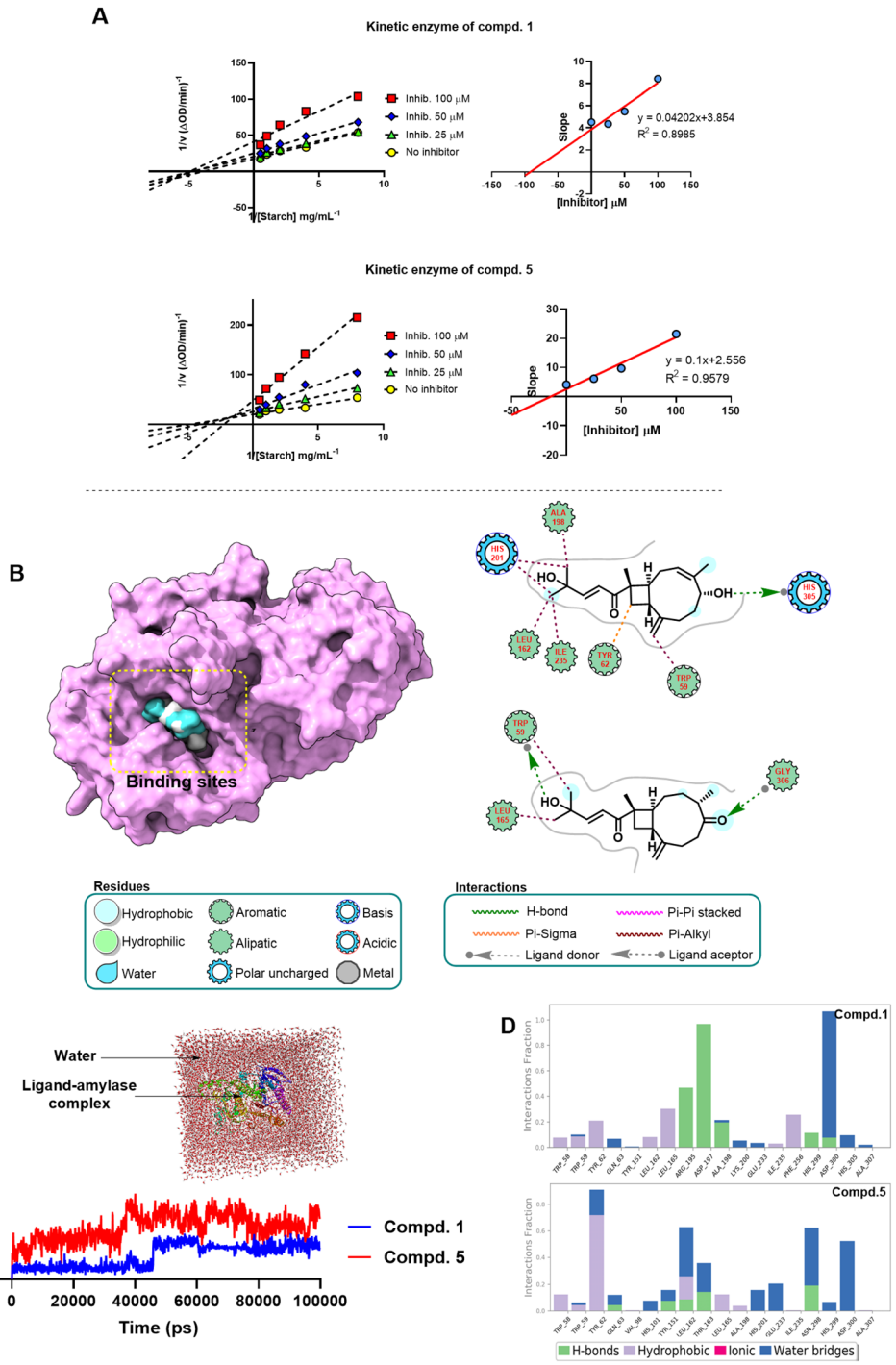

Fig. 8 Lineweaver–Burk plots of the inhibition kinetics (left) and slope *versus* inhibitor concentration plots (right) for the α-amylase enzyme inhibition assay (A). Molecular docking models of the tested compounds at the active site of α-amylase (compound **1** represented by a cyan surface and compound **5** by a gray surface) (B). Molecular dynamics of the ligand–protein complexes is presented alongside the RMSD plots over a 100 ns simulation period (C). The protein–ligand contact maps illustrate the interactions formed throughout the molecular dynamics simulation (D).

Asp300 (51%), and –C^5=O–HOH–Asn298 (42%) (Fig. 8D). These findings provide valuable insights into the conformational stability and ligand–protein interactions critical for inhibitory activity.[45]

Regarding α-glucosidase inhibition, compounds **1–6** showed moderate activity with IC_{50} values below 500 μM, whereas compounds **7–9** exhibited markedly weaker effects. Among them, compound **2** demonstrated the most potent α-glucosidase inhibition (IC_{50} = 241.8 ± 1.11 μM). However, it was 1.67-fold weaker than the commercial drug acarbose (IC_{50} = 144.0 ± 1.99 μM) (Table 4).

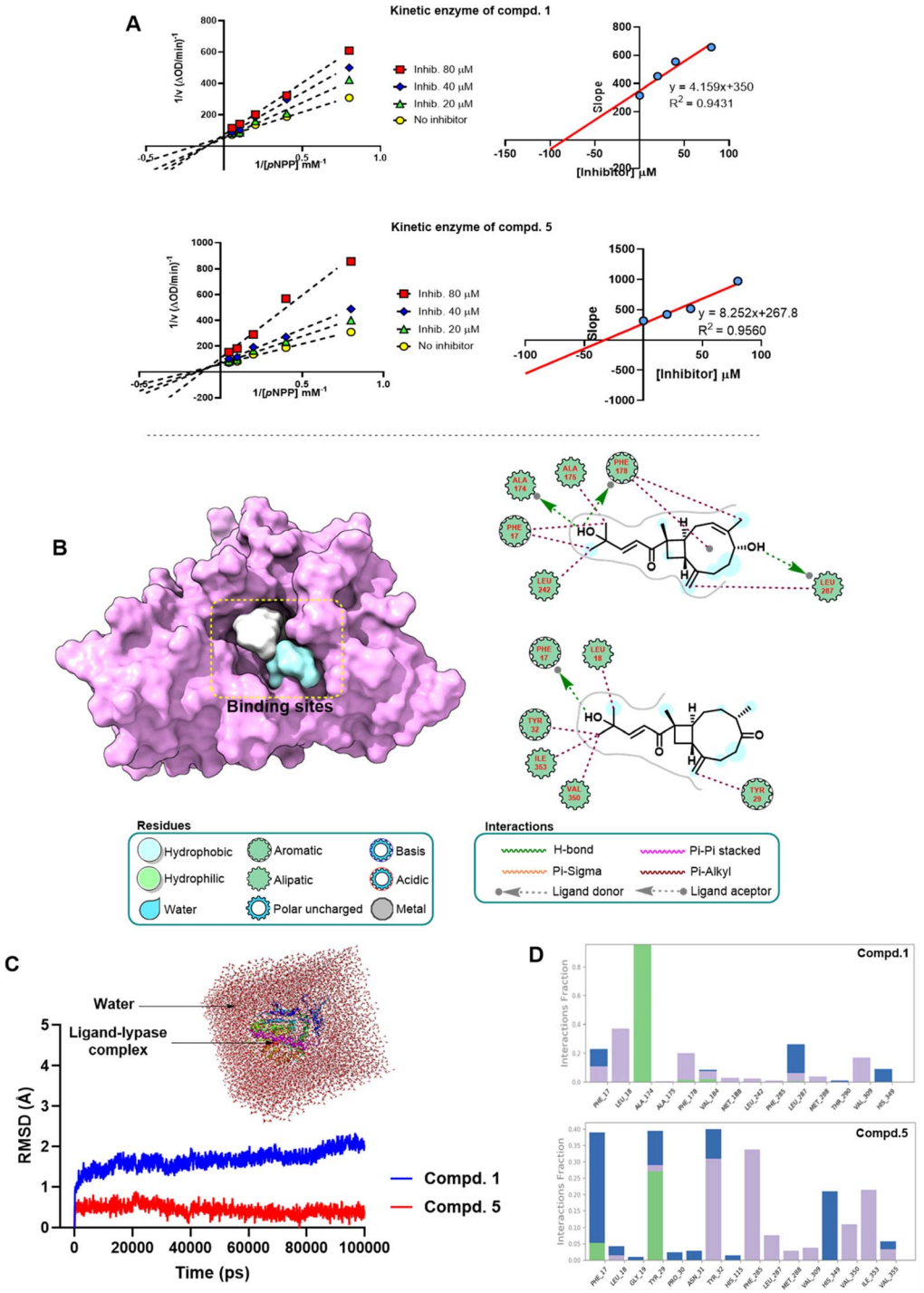

Fig. 9 Lineweaver–Burk plots of the inhibition kinetics (left) and slope *versus* inhibitor concentration plots (right) for the lypase enzyme inhibition assay (A). Molecular docking models of the tested compounds at the active site of lypase (compound **1** represented by a cyan surface and compound **5** by a gray surface) (B). Molecular dynamics of the ligand–protein complexes is presented alongside the RMSD plots over a 100 ns simulation period (C). The protein-ligand contact maps illustrate the interactions formed throughout the molecular dynamics simulation (D).

In the pancreatic lipase inhibition assay, compounds **1** and **5** exhibited the highest potencies with IC_{50} values of 16.1 ± 2.15 and 16.9 ± 1.20 µM, respectively, comparable to the reference inhibitor orlistat (14.2 µM), suggesting strong potential for modulating lipid absorption. Conversely, compounds **6–9** showed negligible lipase inhibition with IC_{50} values exceeding 500 µM. Further enzyme kinetic studies confirmed that compounds **1** and **5** inhibit pancreatic lypase *via* a non-competitive mechanism with K_i values of 84.2 and 32.5 µM, respectively, as determined from Lineweaver–Burk plots (Fig. 9A). At the active site of pancreatic lipase, compounds **1** and **5** exhibited distinct and characteristic interaction patterns.

Table 5 Molecular docking results target α-amylase and lypase

	α-amylase (ID PDB 1B2Y)		Lypase (ID PDB 1EX9)	
Compd.	LC (kJ mol^{-1})[a]	H-bond[b]	LC (kJ mol^{-1})[a]	H-bond[b]
1	−10.16	His305 (3.96)	−9.27	Leu287 (3.70), Phe178 (3.79), Ala174 (3.50)
5	−8.71	Gly306 (3.65), Trp59 (3.73)	−5.79	Phe17 (5.27)

[a] Lipophilic contribution score (kJ mol^{-1}). [b] The numbers in parentheses indicate the bond lengths (Å).

Specifically, compound **1** demonstrated a strong binding affinity within the lipase active pocket with a binding energy of −9.27 kJ mol^{-1} (Table 5 and Fig. 9B). Notable HBD interactions were observed between the C^{15}–OH group and residues Phe178 and Ala174, along with an HBA interaction involving the –OH–linked bicyclo[7.2.0] moiety and Leu287. Additionally, multiple pi–alkyl hydrophobic interactions were formed with aliphatic residues such as Phe17, Ala275, and Leu242. In contrast, compound **5** (−5.79 kJ mol^{-1}) showed a single HBD interaction between C^{15}–OH and Phe17, as well as several pi–alkyl interactions involving aliphatic amino acids Leu18, Ile353, Val350, and aromatic residues Tyr29 and Tyr32 (Fig. 9B). Molecular dynamics simulations revealed that both ligand–protein complexes were highly stable, exhibiting greater stability compared to their respective amylase complexes (Fig. 9C). The **1**-lipase complex stabilized rapidly within 10 ns, maintaining RMSD values between 1.5 and 2.0 Å throughout the simulation. Meanwhile, the **5**-lipase complex displayed exceptional stability, with RMSD values consistently below 0.9 Å over 100 ns of simulation. This enhanced stability is attributed to the extensive hydrophobic interactions formed within the ligand–protein complex. Complex of **1**-lypase formed strong hydrogen bonds between the C^{15}–OH–Ala174 (95%), complemented by hydrophobic contacts with Leu18 (39%), Phe178 (19%), and Val309 (18%). The **5**-lypase complex exhibited hydrogen bonding *via* C^{15}–OH mediated water bridges to Phe17 (6%) (C^{15}–OH–HOH–Phe17) and C^{12}═O–HOH–Tyr29 (26%), along with hydrophobic interactions involving Phe285 (34%), Ile353 (23%), Val350 (12%), and water-mediated contacts at Tyr29 (27%) (C^{16}–HOH–Tyr29) (Fig. 9D). These molecular docking and molecular dynamic results reveal that both compounds employ a combination of polar and nonpolar interactions to engage key residues in the catalytic sites of lipase and amylase, which is critical for potent enzyme inhibition.

The present study highlights the promising potential of compounds **1** and **5** as dual inhibitors targeting key enzymes involved in carbohydrate and lipid metabolism, namely α-amylase and pancreatic lipase. The negligible activity of compounds **6–9** on α-amylase and lypase reinforces the importance of structural features present in compounds **1** and **2** for effective inhibition. The enzyme kinetics analyses demonstrated that compounds **1** and **5** act as non-competitive inhibitors of α-amylase, implying that they bind to allosteric sites rather than directly competing with the substrate at the catalytic site. Their non-competitive inhibition mechanism may translate into beneficial pharmacodynamics, including longer duration of action and reduced side effects related to substrate competition. Molecular docking and dynamics simulations provided mechanistic insights into the interaction of these compounds with α-amylase and lypase. These observations provide detailed insights into the molecular basis of enzyme inhibition by compounds **1** and **5**, highlighting the role of both hydrogen bonding and hydrophobic interactions in stabilizing the complexes, which likely contribute to their inhibitory efficacy against pancreatic lipase and amylase. Future investigations should focus on detailed structure–activity relationship (SAR) studies to optimize these compounds for higher potency and selectivity. Given the multifactorial nature of diabetes and obesity, compounds with dual enzymatic targets present an exciting therapeutic avenue, potentially improving treatment outcomes by addressing multiple metabolic pathways simultaneously.

3.3. Cytotoxic effects and structure–activity relationship analysis (SAR)

The cytotoxic activities of compounds **1–9** were systematically evaluated against the MIA PaCa-2, Panc-1, and KPC cell lines. Compounds **1–5** possess a xeniaphyllane skeleton, whereas compounds **6–9** are characterized by a norcaryophyllene framework. Previous investigations have reported cytotoxic effects of certain representatives within these classes on cancer cell lines such as Hepa59T and KB, with the lowest recorded IC_{50} value being 4.6 μg mL^{-1} against Hepa59T cells.[46] To the best of our knowledge, there are no existing studies examining the effects of similar compounds on MIA PaCa-2, Panc-1, and KPC cell lines. Based on this background and our preliminary experience, an initial screening concentration of 50 μM was

Table 6 Cytotoxic activities against

	IC_{50} (μM)		
Sample	MIA PaCa-2	Panc-1	KPC
1	11.01 ± 1.43	19.06 ± 0.28	17.86 ± 0.87
2	4.97 ± 0.56	8.51 ± 1.21	12.66 ± 1.25
3	**2.52 ± 0.27**	**6.03 ± 0.58**	**5.98 ± 0.78**
4	**2.54 ± 0.38**	**5.24 ± 0.89**	**7.67 ± 0.39**
5	4.07 ± 0.74	7.25 ± 0.23	11.99 ± 1.65
6	>50	>50	>50
7	>50	>50	>50
8	>50	>50	>50
9	>50	>50	>50
Gemcitabine[a]	7.83 ± 0.28	11.58 ± 0.56	5.36 ± 0.25

[a] Positive control.

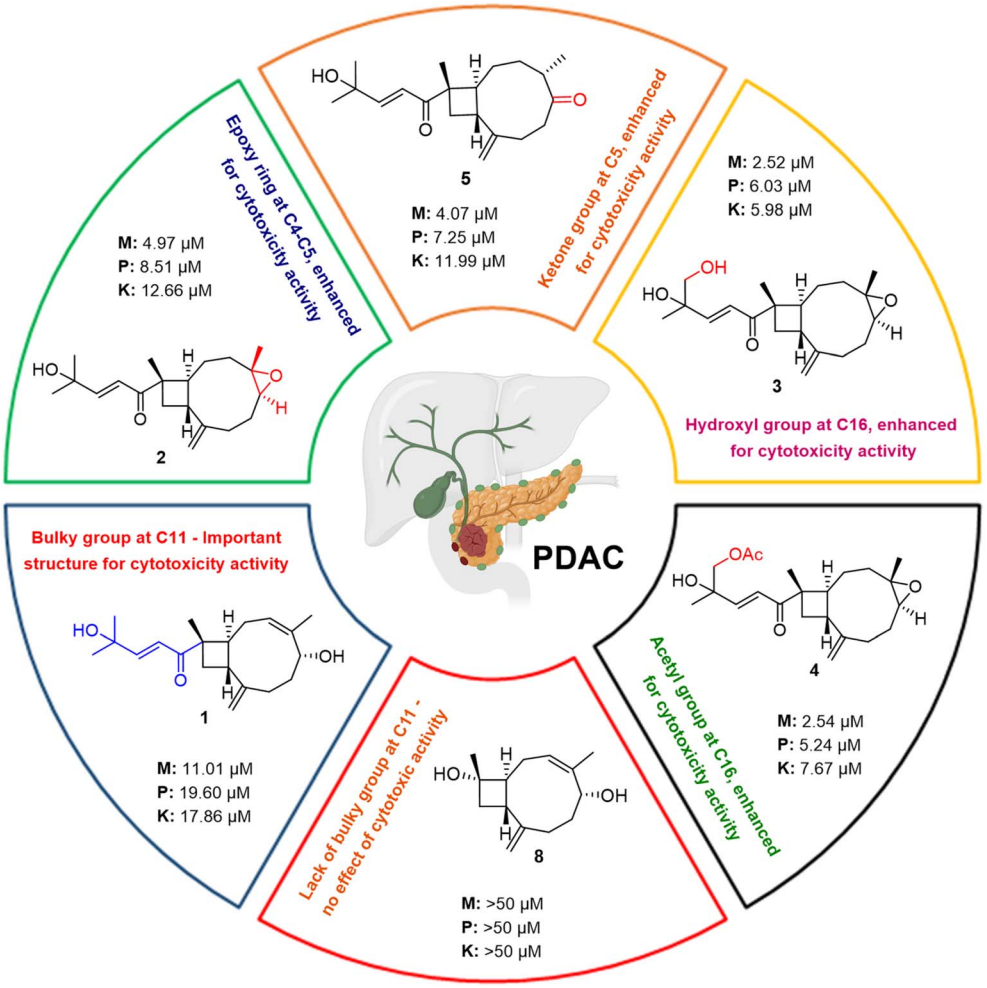

Fig. 10 Structure and cytotoxicity IC_{50} values for SAR analysis of compounds **1–9**.

selected. Compounds exhibiting more than 50% cytotoxicity at this concentration were subsequently subjected to IC_{50} determination.

As summarized in Table 6, compounds **1–5** demonstrated significant cytotoxic activity, with IC_{50} values ranging from 2.54 to 19.60 μM. Notably, in the MIA PaCa-2 cell line, compounds **2–5** exhibited the highest potency, with IC_{50} values between 2.52 and 4.97 μM, surpassing the efficacy of the positive control, gemcitabine, which had an IC_{50} of 7.83 μM. Compound **1** showed moderate inhibitory effects on MIA PaCa-2 cells, with an IC_{50} of 11.01 μM. In the Panc-1 cell line, compounds **2–5** again demonstrated the strongest activity, with IC_{50} values from 5.24 to 7.67 μM, outperforming gemcitabine, which exhibited an IC_{50} of 11.58 μM. Compound **1** also exerted relatively potent inhibition against Panc-1 cells, with IC_{50} values around 19.06 μM. However, the cytotoxic effects observed in Panc-1 and KPC cell lines were notably less pronounced compared to MIA PaCa-2. Conversely, compounds **6–9**, which feature the norcaryophyllene scaffold lacking bulky substituents at the C-11 position, showed negligible inhibitory activity across all three cell lines, with IC_{50} values exceeding 50 μM.

Structural and cytotoxicity data depicted in Fig. 10 reveal a pronounced SAR linked to substituent presence at the C-11 position. While the bicyclo[7.2.0]undecane core framework remains conserved, the introduction of bulky substituents at C-11 critically enhances cytotoxic potency. Specifically, compounds **1–5** bear bulky groups at C-11 with hydroxyl (–OH) or acetoxy (–OAc) functionalities at C-16, corresponding to significantly improved cytotoxicity across MIA PaCa-2, Panc-1, and KPC cell lines, with IC_{50} values between 2.54 and 19.60 μM. Notably, compound **3**, which includes a hydroxyl (–OH) group at the C-16 position, exhibited the highest activity (IC_{50} = 2.52 μM for MIA PaCa-2, 6.03 μM for Panc-1, and 5.98 μM for KPC), underscoring the advantageous role of this substituent. Similarly, compounds **4** and **5** demonstrated potent cytotoxic effects, predominantly with IC_{50} values below 6 μM, reinforcing the significance of C-11 substituent bulkiness in activity enhancement. Furthermore, the obvious difference in the structure of compound **1** compared to compounds **2–4** is the presence of epoxy rings at the C-4 and C-5 positions on the cyclononane ring, which significantly increases the inhibitory activity against all three tested cell lines. Besides that, the ketone group at position C-5 of compound **5** also contributed to the inhibitory effect on cell lines, but not significantly.

In contrast, compounds **6–9**, which lack bulky substituents at C-11 despite retaining the bicyclo[7.2.0]undecane skeleton,

showed no measurable cytotoxicity. This stark differential supports the hypothesis that bulky substituents at C-11 are essential for cytotoxity efficacy, likely due to steric and electronic influences that facilitate molecular recognition and binding at the biological target site. Collectively, this SAR analysis elucidates that the cytotoxic potency of bicyclo[7.2.0] undecane-based compounds is intimately associated with the presence and nature of substituents at C-11. Consequently, strategic modification and optimization of bulky groups at this position represent a promising direction for the development of enhanced anticancer agents.

4. Conclusion

This study involved bioactivity-guided isolation of compounds from *Sclerophytum humesi*, leading to the discovery of two new compounds (**1** and **6**) and seven known compounds (**2–5**, **7–9**). The biological activities, including antidiabetic and cytotoxic effects, were assessed, and preliminary structure–activity relationships were analyzed. Notably, compound **1** exhibited significant inhibitory activity against enzymes central to diabetes pathophysiology, such as α-amylase, α-glucosidase, and lipase. Furthermore, it demonstrated potent cytotoxicity against pancreatic cancer cell lines. Additionally, compounds **3** and **4** showed strong inhibitory activity against MIA PaCa-2, Panc-1, and KPC cells. Mechanistic insights, supported by enzyme kinetics, molecular docking, and molecular dynamics simulations, reveal that both compounds employ a combination of polar and nonpolar interactions to engage key residues in the catalytic sites of lipase and amylase, which is critical for potent enzyme inhibition. These findings suggest that marine-derived terpenoids, such as those studied here, hold promise as dual-function agents targeting both diabetes and pancreatic cancer.

Author contributions

Phuong Vu Luu: conceptualization, investigation, data curation, writing – review & editing. Quoc-Dung Tran Huynh: formal analysis, methodology, validation. Ngoc-Thac Pham: formal analysis, methodology, validation. Huong-Giang Le: formal analysis, methodology, validation, writing – review & editing. Lo-Yun Chen: formal analysis, methodology, validation. Cuong-Quoc Nguyen: formal analysis, methodology, validation. Huong Lien Ton-Nu: data curation, formal analysis, methodology, validation. Mei-Hsien Lee: formal analysis, methodology, validation. Yu-Chia Chang: formal analysis, methodology, validation. Jui-Hsin Su: formal analysis, methodology, validation. Bo-Rong Peng: conceptualization, supervision, formal analysis, methodology, validation. Kuei-Hung Lai: conceptualization, funding acquisition, supervision, writing – review & editing.

Conflicts of interest

The authors declare that they have no known competing financial interests or personal relationships that could have appeared to influence the work reported in this paper.

Data availability

The data supporting this study have been provided within the SI Section. Supplementary information is available. See DOI: https://doi.org/10.1039/d5ra04971g.

Acknowledgements

This work was supported by the National Science and Technology Council of Taiwan (MOST 111-2320-B-038-040-MY3, 113-2628-B-038-009-MY3, 113-2321-B-255-001, and 114-2326-B-038-002-MY3); and from the Ministry of Education (DP2-TMU-114-C-06).

Notes and references

1 D. Li, Diabetes and pancreatic cancer, *Mol. Carcinog.*, 2012, **51**(1), 64–74, DOI: 10.1002/mc.20771.
2 F. Amri, C. Belkhayat, A. yeznasni, H. Koulali, R. Jabi, A. Zazour, N. Abda, M. Bouziane, Z. Ismaili and G. Kharrasse, Association between pancreatic cancer and diabetes: insights from a retrospective cohort study, *BMC Cancer*, 2023, **23**(1), 856, DOI: 10.1186/s12885-023-11344-w.
3 T. Salvatore, R. Marfella, M. R. Rizzo and F. C. Sasso, Pancreatic cancer and diabetes: A two-way relationship in the perspective of diabetologist, *Int. J. Surg.*, 2015, **21**(1), S72–S77, DOI: 10.1016/j.ijsu.2015.06.063.
4 Q. Ben, M. Xu, X. Ning, J. Liu, S. Hong, W. Huang, H. Zhang and Z. Li, Diabetes mellitus and risk of pancreatic cancer: A meta-analysis of cohort studies, *Eur. J. Cancer*, 2011, **47**(13), 1928–1937, DOI: 10.1016/j.ejca.2011.03.003.
5 L. M. Rodriguez, C. S. Cendra, M. P. Gonzalez, D. G. Abad, I. J. Martel and M. De Torres Olombrada, Pancreatic ductal adenocarcinoma (PDAC) and type 2 diabetes mellitus: Cause or consequence? Analysis of the prevalence of alterations in glucose metabolism (AGM) in a patients' cohort with PDAC, *Ann. Oncol.*, 2018, **29**, v40, DOI: 10.1093/annonc/mdy151.143.
6 A. M. Y. Zhang, Y. H. Xia, J. S. H. Lin, K. H. Chu, W. C. K. Wang, T. J. J. Ruiter, J. C. C. Yang, N. Chen, J. Chhuor, S. Patil, H. H. Cen, E. J. Rideout, V. R. Richard, D. F. Schaeffer, R. P. Zahedi, C. H. Borchers, J. D. Johnson and J. L. Kopp, Hyperinsulinemia acts via acinar insulin receptors to initiate pancreatic cancer by increasing digestive enzyme production and inflammation, *Cell Metab.*, 2023, **35**(12), 2119–2135, DOI: 10.1016/j.cmet.2023.10.003.
7 B. Schludi, A. S. M. Moin, C. Montemurro, T. Gurlo, A. V. Matveyenko, D. Kirakossian, D. W. Dawson, S. M. Dry, P. C. Butler and A. E. Butler, Islet inflammation and ductal proliferation may be linked to increased pancreatitis risk in type 2 diabetes, *JCI Insight*, 2017, **2**(13), e92282, DOI: 10.1172/jci.insight.92282.
8 M. H. Jensen, S. L. Cichosz, O. Hejlesen, S. D. Henriksen, A. M. Drewes and S. S. Olesen, Risk of pancreatic cancer in people with new-onset diabetes: A Danish nationwide

population-based cohort study, *Pancreatology*, 2023, **23**(6), 642–649, DOI: 10.1016/j.pan.2023.07.001.

9 J. S. Bhatti, A. Sehrawat, J. Mishra, I. S. Sidhu, U. Navik, N. Khullar, S. Kumar, G. K. Bhatti and P. H. Reddy, Oxidative stress in the pathophysiology of type 2 diabetes and related complications: Current therapeutics strategies and future perspectives, *Free Radic. Biol. Med.*, 2022, **184**, 114–134, DOI: 10.1016/j.freeradbiomed.2022.03.019.

10 S. Tangvarasittichai, Oxidative stress, insulin resistance, dyslipidemia and type 2 diabetes mellitus, *World J. Diabetes*, 2015, **6**(3), 456–480, DOI: 10.4239/wjd.v6.i3.456.

11 O. O. Oguntibeju, Type 2 diabetes mellitus, oxidative stress and inflammation: examining the links, *Int. J. Physiol., Pathophysiol. Pharmacol.*, 2019, **11**(3), 45–63.

12 H. Yousef, A. H. Khandoker, S. F. Feng, C. Helf and H. F. Jelinek, Inflammation, oxidative stress and mitochondrial dysfunction in the progression of type II diabetes mellitus with coexisting hypertension, *Front. Endocrinol.*, 2023, **14**, 1173402, DOI: 10.3389/fendo.2023.1173402.

13 J. Gong, X. Li, Z. Feng, J. Lou, K. Pu, Y. Sun, S. Hu, Y. Zhou, T. Song, M. Shangguan, K. Zhang, W. Lu, X. Dong, J. Wu, H. Zhu, Q. He, H. Xu and Y. Wu, Sorcin can trigger pancreatic cancer-associated new-onset diabetes through the secretion of inflammatory cytokines such as serpin E1 and CCL5, *Exp. Mol. Med.*, 2024, **56**(11), 2535–2547, DOI: 10.1038/s12276-024-01346-4.

14 R. Weinberg Sibony, O. Segev, S. Dor and I. Raz, Overview of oxidative stress and inflammation in diabetes, *J. Diabetes*, 2024, **16**(10), e70014, DOI: 10.1111/1753-0407.70014.

15 P. P. Khin, J. H. Lee and H.-S. Jun, Pancreatic Beta-cell Dysfunction in Type 2 Diabetes, *Eur. J. Inflamm.*, 2023, **21**, 1721727X231154152, DOI: 10.1177/1721727x231154152.

16 P. Newsholme, K. N. Keane, R. Carlessi and V. Cruzat, Oxidative stress pathways in pancreatic β-cells and insulin-sensitive cells and tissues: importance to cell metabolism, function, and dysfunction, *Am. J. Physiol. Cell Physiol.*, 2019, **317**(3), C420–c433, DOI: 10.1152/ajpcell.00141.2019.

17 B. Duvillié, R. Kourdoughli, S. Druillennec, A. Eychène and C. Pouponnot, Interplay Between Diabetes and Pancreatic Ductal Adenocarcinoma and Insulinoma: The Role of Aging, Genetic Factors, and Obesity, *Front. Endocrinol.*, 2020, **11**, 563267, DOI: 10.3389/fendo.2020.563267.

18 D. K. Andersen, M. Korc, G. M. Petersen, G. Eibl, D. Li, M. R. Rickels, S. T. Chari and J. L. Abbruzzese, Diabetes, Pancreatogenic Diabetes, and Pancreatic Cancer, *Diabetes*, 2017, **66**(5), 1103–1110, DOI: 10.2337/db16-1477.

19 R. Subramanian, M. Z. Asmawi and A. Sadikun, In vitro alpha-glucosidase and alpha-amylase enzyme inhibitory effects of Andrographis paniculata extract and andrographolide, *Acta Biochim. Pol.*, 2008, **55**(2), 391–398.

20 K. R. Zhuang, C. F. Chen, H. Y. Chan, S. E. Wang, D. H. Lee, S. C. Chen, B. U. Shyr, Y. J. Chou, C. C. Chen, S. H. Yuan, Y. I. Chang, H. T. Lee and S. L. Fu, Andrographolide suppresses the malignancy of pancreatic cancer via alleviating DNMT3B-dependent repression of tumor suppressor gene ZNF382, *Phytomedicine*, 2024, **132**, 155860, DOI: 10.1016/j.phymed.2024.155860.

21 M. Foddai, V. Kasabri, G. L. Petretto, E. Azara, A. Sias, F. U. Afifi, G. Delogu, M. Chessa and G. Pintore, In vitro Inhibitory Effects of Limonium contortirameum and L. virgatum Extracts from Sardinia on α-Amylase, α-Glucosidase and Pancreatic Lipase, *Nat. Prod. Commun.*, 2014, **9**(2), 1934578X1400900212, DOI: 10.1177/1934578x1400900212.

22 C. F. Chiu, H. Y. Chang, C. Y. Huang, C. Z. Mau, T. T. Kuo, H. C. Lee and S. Y. Huang, Betulinic Acid Affects the Energy-Related Proteomic Profiling in Pancreatic Ductal Adenocarcinoma Cells, *Molecules*, 2021, **26**(9), 2482, DOI: 10.3390/molecules26092482.

23 S. Thengyai, P. Thiantongin, C. Sontimuang, C. Ovatlarnporn and P. Puttarak, α-Glucosidase and α-amylase inhibitory activities of medicinal plants in Thai antidiabetic recipes and bioactive compounds from Vitex glabrata R. Br. stem bark, *J. Herb. Med.*, 2020, **19**, 100302.

24 D. Tan, H. H. L. Tseng, Z. Zhong, S. Wang, C. T. Vong and Y. Wang, Glycyrrhizic Acid and Its Derivatives: Promising Candidates for the Management of Type 2 Diabetes Mellitus and Its Complications, *Int. J. Mol. Sci.*, 2022, **23**(19), 10988, DOI: 10.3390/ijms231910988.

25 M. Minekus, M. Alminger, P. Alvito, S. Ballance, T. Bohn, C. Bourlieu, F. Carrière, R. Boutrou, M. Corredig and D. Dupont, A standardised static in vitro digestion method suitable for food–an international consensus, *Food Funct.*, 2014, **5**(6), 1113–1124.

26 N. N. Tuan, H. N. Thi, C. L. T. My, T. X. Hai, H. T. Trung, A. N. T. Kim, T. N. Tan, T. L. Van, C. Q. Nguyen and Q. D. Tran, Inhibition of α-glucosidase, acetylcholinesterase, and nitric oxide production by phytochemicals isolated from Millettia speciosa—In vitro and molecular docking studies, *Plants*, 2022, **11**(3), 388.

27 F. Rashid, M. Ahmad, U. A. Ashfaq, A. A. Al-Mutairi and S. A. Al-Hussain, Design, synthesis and pharmacological evaluation of 2-(3-benzoyI-4-hydroxy-1, 1-dioxido-2H-benzo [e][1, 2] thiazin-2-yI)-N-(2-bromophenyl) acetamide as antidiabetic agent, *Drug Des. Dev. Ther.*, 2022, 4043–4060.

28 D. Ganavi, S. Patil, V. Kumar, R. Ramu and B. Poojary, Pyrazole-imidazopyridine hydrazones: synthesis, α-glucosidase, α-amylase inhibitory activity and computational studies, *ChemistrySelect*, 2023, **8**, e202300778.

29 N. Abdelriheem, Y. Zaki and A. Abdelhamid, Synthesis of some new pyrazolo [1, 5-a] pyrimidine, pyrazolo [5, 1-c] triazine, 1,3,4-thiadiazole and pyridine derivatives containing 1,2,3-triazole moiety, *Chem. Cent. J.*, 2017, **11**, 1.

30 Q. Le Dang, C. Quoc Nguyen, Q. De Tran, J. C. Kim, K. A. Thi Vo, H. Thi Cao, X. Thi Nguyen, T. Huy Nguyen, T. T. Thi Nguyen and T. Huu Nguyen, Anti-Phytopathogenic and Phytotoxic Effects of *Annona glabra* Lin. and *Annona muricata* Lin. Seed Extracts: In vitro and In vivo Assessment, Bioactive Compound Quantification, and Mechanism Involved, *ChemistrySelect*, 2024, **9**(30), e202401730.

31 T. Q. De, C. Q. Nguyen, Q. Le Dang, N. Y. N. Thi, N. T. Tuan, D. H. Suh, J. Chu, S. Bepary, G. H. Lee and N. S. Kang, Rational design of novel diaryl ether-linked benzimidazole derivatives as potent and selective BACE1 inhibitors, *Biochem. Biophys. Res. Commun.*, 2024, **698**, 149538.

32 H. P. Nguyen, Q. De Tran, C. Q. Nguyen, T. P. Hoa, T. D. Binh, H. N. Thao, B. T. B. Hue, N. T. Tuan, Q. Le Dang and N. Q. C. Thanh, Anti-multiple myeloma potential of resynthesized belinostat derivatives: An experimental study on cytotoxic activity, drug combination, and docking studies, *RSC Adv.*, 2022, **12**(34), 22108–22118.

33 H. Nguyen-Ngoc, C. Q. Nguyen, K. A. T. Vo, T. T. T. Nguyen, D. T. Nghiem, N. T. Ha, V. M. Nguyen, G. J. Choi, A. G. Ardiansyah and C. T. Nguyen, Insight into the role of phytoalexin naringenin and phytohormone abscisic acid in defense against phytopathogens Phytophthora infestans and Magnaporthe oryzae: In vitro and in silico approaches, *Physiol. Mol. Plant Pathol.*, 2023, **127**, 102123.

34 B. T. B. Hue, H. N. H. Giang, C. Q. Nguyen, F.-P. Chou, D. L. D. Thanh, Q. De Tran, V. T. Hieu, L. H. P. Mai, H.-C. Lin and T.-K. Wu, Discovery of a novel benzimidazole conjugated quinazolinone derivative as a promising SARS-CoV-2 3CL protease inhibitor, *RSC Adv.*, 2024, **14**(46), 33820–33829.

35 V. Nahoum, G. Roux, V. Anton, P. Rouge, A. Puigserver, H. Bischoff, B. Henrissat and F. Payan, Crystal structures of human pancreatic α-amylase in complex with carbohydrate and proteinaceous inhibitors, *Biochem. J.*, 2000, **346**(1), 201–208.

36 M. Nardini, D. A. Lang, K. Liebeton, K.-E. Jaeger and B. W. Dijkstra, Crystal Structure of Pseudomonas aeruginosa Lipase in the Open Conformation: THE PROTOTYPE FOR FAMILY I.1 OF BACTERIAL LIPASES, *J. Biol. Chem.*, 2000, **275**(40), 31219–31225, DOI: **10.1074/jbc.M003903200**.

37 T. Mosmann, Rapid colorimetric assay for cellular growth and survival: Application to proliferation and cytotoxicity assays, *J. Immunol. Methods*, 1983, **65**(1), 55–63, DOI: **10.1016/0022-1759(83)90303-4**.

38 Z.-J. Tang, Z.-M. Cao, X.-W. Guo, H.-J. Chen, Y. Lian, W.-J. Zheng, Y.-J. Chen, H.-Z. Lian and X. Hu, Cytotoxicity and toxicoproteomic analyses of human lung epithelial cells exposed to extracts of atmospheric particulate matters on PTFE filters using acetone and water, *Ecotoxicol. Environ. Saf.*, 2020, **191**, 110223, DOI: **10.1016/j.ecoenv.2020.110223**.

39 M. Khatri, D. Bello, A. K. Pal, J. M. Cohen, S. Woskie, T. Gassert, J. Lan, A. Z. Gu, P. Demokritou and P. Gaines, Evaluation of cytotoxic, genotoxic and inflammatory responses of nanoparticles from photocopiers in three human cell lines, *Part. Fibre Toxicol.*, 2013, **10**(1), 42, DOI: **10.1186/1743-8977-10-42**.

40 A. F. Ahmed, J.-H. Su, R.-T. Shiue, X.-J. Pan, C.-F. Dai, Y.-H. Kuo and J.-H. Sheu, New β-Caryophyllene-Derived Terpenoids from the Soft Coral Sinularia nanolobata, *J. Nat. Prod.*, 2004, **67**(4), 592–597, DOI: **10.1021/np030286w**.

41 S.-P. Chen, J.-H. Su, A. F. Ahmed, C.-F. Dai, Y.-C. Wu and J.-H. Sheu, Xeniaphyllane-derived terpenoids from the Formosan soft coral Sinularia gibberosa, *Chem. Pharm. Bull.*, 2007, **55**(10), 1471–1475.

42 S.-Q. Lu, X.-W. Li, S.-W. Li, Z. Cui, Y.-W. Guo and G.-Y. Han, Sinuhirtins A and B, two uncommon norhumulene-type terpenoids from the South China Sea soft coral Sinularia hirta, *Tetrahedron Lett.*, 2019, **60**(51), 151308, DOI: **10.1016/j.tetlet.2019.151308**.

43 Y. Li, H. Huang and Y.-W. Guo, A new norsesquiterpene from Hainan soft coral Sinularia sp, *Nat. Prod. Res.*, 2008, **22**(15), 1359–1364, DOI: **10.1080/14786410701773295**.

44 Z.-H. Chen, S.-Q. Lu, G.-Y. Han, X.-W. Li and Y.-W. Guo, Sinuhirtone A, an uncommon 17, 19-dinorxeniaphyllanoid, and nine related new terpenoids from the Hainan soft coral Sinularia hirta, *Mar. Drugs*, 2022, **20**(4), 272.

45 W. R. Abraham, L. Ernst and B. Stumpf, *Phytochemistry*, 1990, **29**, 120.

46 M. Abdul Basith Khan, M. J. Hashim, J. K. King, R. D. Govender, H. Mustafa and J. Al Kaabi, Epidemiology of Type 2 Diabetes — Global Burden of Disease and Forecasted Trends, *J. Epidemiol. Glob. Health*, 2020, **10**(1), 107–111, DOI: **10.2991/jegh.k.191028.001**.